The Astronomical Journal, 157:224 (10pp), 2019 June https://doi.org/10.3847/1538-3881/ab19bc

Qatar Exoplanet Survey: Qatar-8b, 9b, and 10b—A Hot Saturn and Two Hot Jupiters

Khalid Alsubai[1], Zlatan I. Tsvetanov[1], Stylianos Pyrzas[1], David W. Latham[2], Allyson Bieryla[2], Jason Eastman[2], Dimitris Mislis[1], Gilbert A. Esquerdo[2], John Southworth[3], Luigi Mancini[4,5,6,7], Ali Esamdin[8], Jinzhong Liu[8], Lu Ma[8], Marc Bretton[9], Enric Pallé[10,11], Felipe Murgas[10,11], Nicolas P. E. Vilchez[1], Hannu Parviainien[10,11], Pilar Montañes-Rodriguez[10,11], Norio Narita[10,12,13,14,15], Akihiko Fukui[10,16], Nobuhiko Kusakabe[13], Motohide Tamura[12,13], Khalid Barkaoui[17,18], Francisco Pozuelos[17], Michael Gillon[17], Emmanuel Jehin[17], Zouhair Benkhaldoun[18], and Ahmed Daassou[18]

[1] Hamad bin Khalifa University (HBKU), Qatar Foundation, P.O. Box 5825, Doha, Qatar; kalsubai@qf.org.qa
[2] Harvard-Smitsonian Center for Astrophysics, 60 Garden Street, Cambridge, MA 02138, USA
[3] Astrophysics Group, Keele University, Staffordshire ST5 5BG, UK
[4] Department of Physics, University of Rome Tor Vergata, Via della Ricerca Scientifica 1, I-00133 Roma, Italy
[5] Max Planck Institute for Astronomy, Königstuhl 17, D-69117 Heidelberg, Germany
[6] INAF-Osservatorio Astrofisico di Torino, Via Osservatorio 20, I-10025 Pino Torinese, Italy
[7] International Institute for Advanced Scientific Studies (IIASS), Via G. Pellegrino 19, I-84019 Vietri sul Mare (SA), Italy
[8] Xinjiang Astronomical Observatory (XAO), Chinese Academy of Sciences, 150 Science 1-Street, Urumqi, Xinjiang 830011, People's Republic of China
[9] Observatoire des Baronnies Provençales (OBP), Le Mas des Grés, Route de Nyons, F-05150 Moydans, France
[10] Instituo de Astrofísica da Canarias (IAC), E-38205 La Laguna, Tenerife, Spain
[11] Departamento de Astrofísica, Universidad de La Laguna (ULL), E-38206 La Laguna, Tenerife, Spain
[12] Department of Astronomy, Graduate School of Science, The University of Tokyo, 7-3-1 Hongo, Bunkyo-ku, Tokyo 113-0033, Japan
[13] Astrobiology Center, National Institutes of Natural Sciences, 2-21-1 Osawa, Mitaka, Tokyo 181-8588, Japan
[14] JST, PRESTO, 7-3-1 Hongo, Bunkyo-ku, Tokyo 113-0033, Japan
[15] National Astronomical Observatory of Japan, 2-21-1 Osawa, Mitaka, Tokyo 181-8588, Japan
[16] Department of Earth and Planetary Science, Graduate School of Science, The University of Tokyo, 7-3-1 Hongo, Bunkyo-ku, Tokyo 113-0033, Japan
[17] Space sciences, Technologies and Astrophysics Research (STAR) Institute, Université de Liège, Allée du 6 Août 17, Bat. B5C, B-4000, Liège, Belgium
[18] Oukaimeden Observatory, High Energy Physics and Astrophysics Laboratory, Cadi Ayyad University, Marrakech, Morocco
Received 2018 October 18; revised 2019 April 14; accepted 2019 April 14; published 2019 May 10

Abstract

In this paper we present three new extrasolar planets from the Qatar Exoplanet Survey. Qatar-8b is a hot Saturn, with $M_P = 0.37\,M_J$ and $R_P = 1.3\,R_J$, orbiting a solar-like star every $P_{orb} = 3.7$ days. Qatar-9b is a hot Jupiter with a mass of $M_P = 1.2\,M_J$ and a radius of $R_P = 1\,R_J$, in an orbit of $P_{orb} = 1.5$ days around a low mass, $M_\star = 0.7\,M_\odot$, mid-K main-sequence star. Finally, Qatar-10b is a hot, $T_{eq} \sim 2000$ K, sub-Jupiter mass planet, $M_P = 0.7\,M_J$, with a radius of $R_P = 1.54\,R_J$ and an orbital period of $P_{orb} = 1.6$ days, placing it on the edge of the sub-Jupiter desert.

Key words: planetary systems – planets and satellites: detection – planets and satellites: fundamental parameters – techniques: photometric

1. Introduction

Since Mayor & Queloz (1995) announced 51 Peg, the first extrasolar planet around a main-sequence star, the number of extrasolar planets has been rising steadily, revealing the large diversity in physical properties and configurations of the underlying extrasolar planets population. In order to properly understand this diversity, a large sample of well-characterized, in terms of physical properties, planets and their respective host stars is required.

Large-scale, ground-based surveys for transiting extrasolar planets, such as Optical Gravitational Lensing Experiment (OGLE-III; Udalski et al. 2002), Trans-Atlantic Exoplanet Survey (TrES; Alonso et al. 2004), Hungarian Automated Telescope Network (HATNet; Bakos et al. 2004), XO (McCullough et al. 2005), Wide Angle Search for Planets (WASP; Pollacco et al. 2006), Kilodegree Extremely Little Telescope (KELT; Pepper et al. 2007), and Qatar Exoplanet Survey (QES; Alsubai et al. 2013), have played a pivotal role both in significantly increasing the numbers of known planets and in providing prime targets to fulfill the well-characterized requirement. By design, these surveys offer certain advantages: (i) the very fact that the planets are transiting implies that, generally, both the actual mass (M_P, not only $M_P \sin i$) and the planet radius (and by extension, the bulk density) can be determined; (ii) ground-based surveys are more sensitive to brighter host stars and larger planets, which (usually) allows for the physical properties of the planet to be determined with good precision (better than 10%) and offers the possibility of individual systems suitable for intensive follow-up studies.

In this paper we present three new transiting extrasolar planets discovered by QES: Qatar-8b—a hot Saturn around a solar-like star, Qatar-9b—a hot Jupiter orbiting a mid-K main-sequence star, and Qatar-10b—a hot Jupiter around a late-F main-sequence star. The paper is organized as follows. In Section 2 we present the survey photometry and describe the follow-up photometry and spectroscopy used to confirm the planetary nature of the transits. In Section 3 we present the analysis of the data and the global system solutions using simultaneous fits to the available radial velocities (RVs) and follow-up photometric light curves, and in Section 4 we summarize our results and put the three new planets in the broader context of the exoplanets field.

2. Observations

2.1. Discovery Photometry

The survey data were collected with QES, hosted by the New Mexico Skies Observatory[19] located in Mayhill, NM,

[19] http://www.nmskies.com

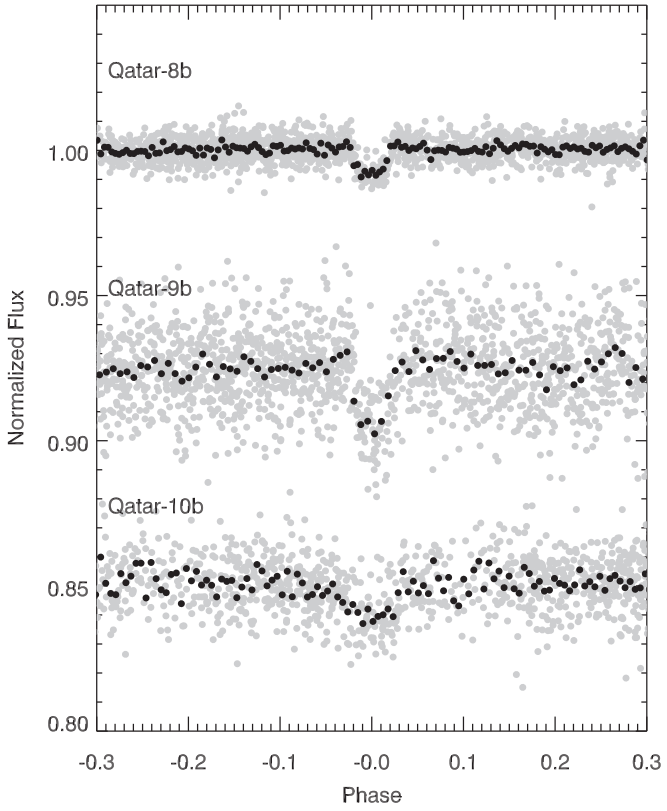

Figure 1. Discovery light curves for Qatar-8b (top), Qatar-9b (middle), and Qatar-10b (bottom) folded to the period identified by the BLS analysis and plotted with an arbitrary vertical offset for clarity. The gray points represent the original observations, and the black points are the binned values to better guide the eye.

USA. A full description of QES can be found in our previous publications, e.g., Alsubai et al. (2013, 2017).

The discovery light curves of Qatar-8b and Qatar-9b contain 2959 and 2755 data points, respectively, obtained during observations from 2016 December 5 to 2017 May 9. For Qatar-10b, the discovery light curve has 2077 data points collected in the time period 2017 March 21–November 1. The survey images are run through the QES pipeline, which extracts the photometric measurements using the image subtraction algorithm by Bramich (2008). A full description of the pipeline can be found in Alsubai et al. (2013).

The output light curves are ingested into the QES archive and are detrended using a combination of the `Trend Filtering Algorithm` (TFA; Kovács et al. 2005), which constructs a filter function from a set of field stars considered to be a representative template for systematics in the field, and the `DOHA` algorithm (Mislis et al. 2017), a co-trending algorithm used to eliminate lingering, quasi-systematic patterns identified from groups of stars that are highly correlated to each other. The light curves are then further processed with the `TSARDI` algorithm (Mislis et al. 2018), a machine learning points rejection algorithm that deals with any residual data irregularities. Qatar-8b, 9b, and 10b were identified as strong candidates during a search for transit-like events using the `Box Least Squares` algorithm (BLS) of Kovács et al. (2002), following a procedure similar to that described in Collier Cameron et al. (2006). Note that, although the initial candidate selection is an automatic procedure, the final vetting is done by eye.

Table 1
Log of Follow-up Photometric Observations for Qatar-8b, 9b, and 10b

ID	Date	Telescope	Filter	Cadence, (s)	Rms, (mmag)
Qatar-8b					
1	2018 Apr 2	QFT	*g*	35	2.3
2	2018 Apr 2	FLWO	*i*	30	0.6
3	2018 Apr 5	OBP	*I*	125	1.6
Qatar-9b					
1	2018 Apr 19	QFT	*i*	204	4.2
2	2018 Apr 26	TCS	*g*	30	2.9
3	2018 Apr 26	TCS	*r*	30	1.9
4	2018 Apr 26	TCS	*i*	30	1.9
5	2018 Apr 26	TCS	*z*	30	2.2
6	2018 May 6	FLWO	*g*	35	1.5
7	2018 May 6	QFT	*g*	204	6.0
Qatar-10b					
1	2018 May 9	QFT	*i*	204	3.0
2	2018 May 14	QFT	*g*	204	2.6
3	2018 May 19	QFT	*z*	204	5.1
4	2018 May 19	FLWO	*g*	28	0.9
5	2018 Jul 23	CAHA	*R*	116	1.0
6	2018 Sep 2	OBP	*I*	124	1.1
7	2018 Sep 6	QFT	*i*	204	3.2
8	2018 Sep 14	TRAPPIST-N	*I*	32	1.7

Note. See the text for details on telescopes and instruments. The last columns gives the mean error in two-minute bins.

Figure 1 shows the discovery light curves for the three exoplanets discussed in this paper.

2.2. Follow-up Photometry

Follow-up photometric observations of a number of transits of Qatar-8b, 9b, and 10b were collected at five different observatories with the following combination of telescopes and instruments:

FLWO: the 1.5 m telescope at the Fred L. Whipple Observatory (Mount Hopkins, Arizona, USA) in combination with KeplerCam, equipped with a single 4k × 4k Fairchild CCD with a $0\farcs37$ pixel^{-1} and a $23\farcm1 \times 23\farcm1$ on-sky field of view (FOV).

QFT: the 0.5 m Qatar Follow-up Telescope (New Mexico Skies Observatory, Mayhill, New Mexico, USA), equipped with a 1k × 1k Andor iKon-M 934 CCD, yielding a FOV of $13' \times 13'$.

OBP: the 0.82 m telescope at the Observatoire des Baronnies Provençales[20] (Provence-Alpes-Côte d'Azur, France) equipped with a FLI ProLine PL230 camera with a 2k × 2k e2v CCD detector resulting in a $23' \times 23'$ FOV.

CAHA: the 1.23 m Zeiss telescope at the Centro Astronómico Hispano-Alemán (Calar Alto, Spain) in combination with

[20] http://www.obs-bp.fr

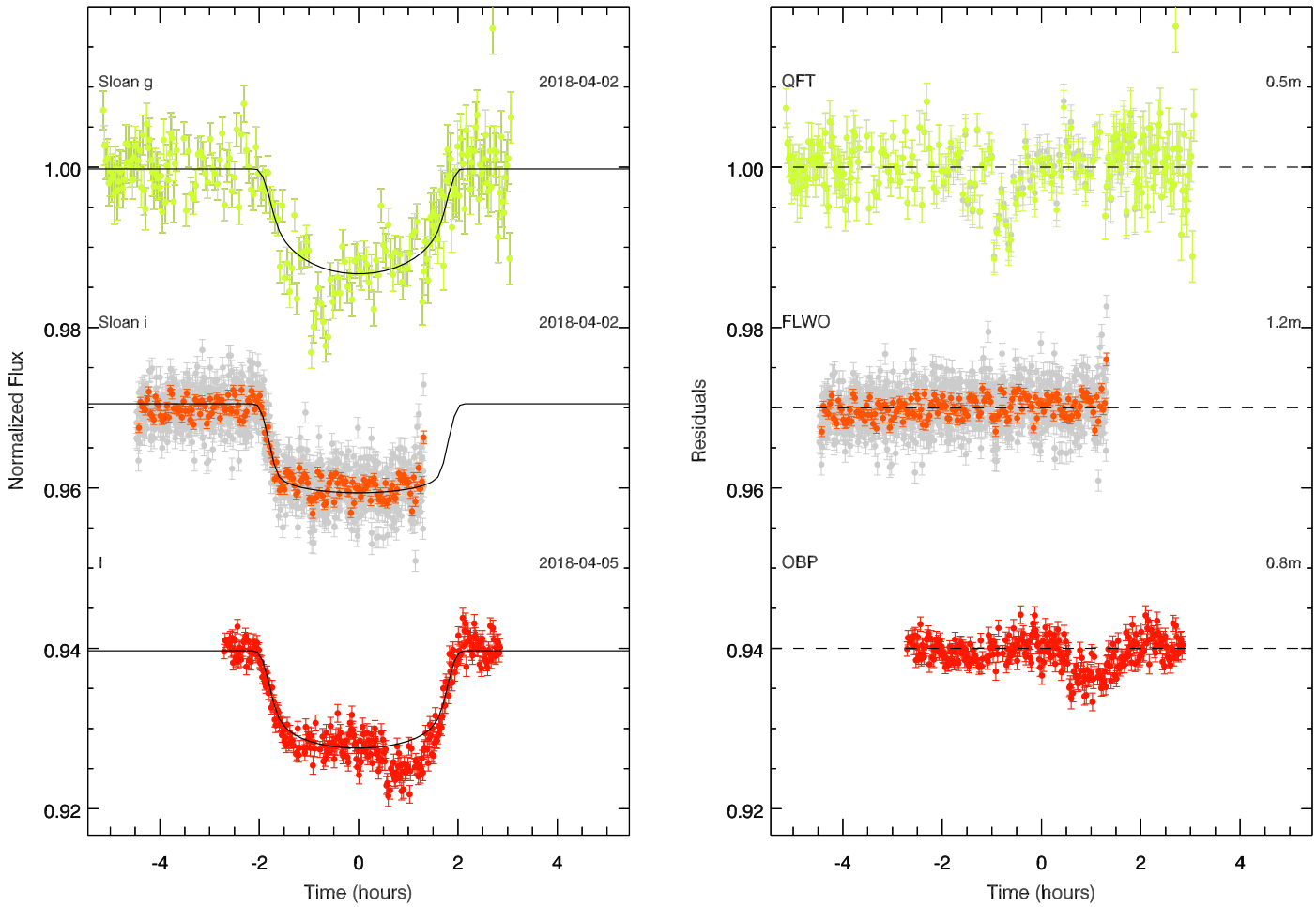

Figure 2. Three follow-up light curves of Qatar-8b. The left panel shows the light curves ordered from top to bottom as they appear in Table 1 with a vertically added shift for clarity. The solid black lines are the best model fits (see Section 3.2). The residuals from the fits are shown in the right panel. The individual data points are color coded according to the filter used and for observations taken with KeplerCam and Muscat2 we show both the original data points (light gray) as well as the data binned to a uniform cadence of 2 minutes. The filter, date of observation, observatory, and telescope size are also given in the two panels.

the DLR-MKIII camera with a 4k × 4k, e2v CCD resulting in a 21′.5 × 21′.5 FOV.

TCS: the 1.52 m Telescopio Carlos Sanchez at the Teide Observatory (Tenerife, Canary Islands, Spain) with the MuSCAT2 instrument, which takes images in four filters simultaneously. Each channel is equipped with a 1k × 1k CCD, resulting in a 7′.4 × 7′.4 on-sky FOV. For a detailed description of MuSCAT2 and its dedicated photometric pipeline see Narita et al. (2019).

TRAPPIST-North: the 0.6 m robotic Transiting Planets and Planetesimals Small Telescope[21] is located at Oukaimeden Observatory, Morocco. It is equipped with a 2k × 2k deep-depletion Andor IKONL BEX2 DD CCD camera with a pixel scale of 0″.60 and an on-sky FOV of 19′.8 × 19′.8.

All of the follow-up light curves were generated through differential aperture photometry performed on the sequence of images for each observing run. In each case a number of comparison stars were selected and those with excessive noise or suspected variability were excluded from the final analysis. For the CAHA observations, the telescope was defocused and data reduction was carried out using the `DEFOT` pipeline (Southworth et al. 2009, 2014). For observations taken at FLWO, OBP, and with QFT the telescope was kept only approximately in focus and we used the AstroImageJ (AIJ) software package (Choi et al. 2016) to extract the light curves. The MuSCAT2 instrument on TCS has a dedicated pipeline for extracting the light curves. The extraction of the fluxes for the TRAPPIST-North observations was done by aperture photometry on selected stars with the IRAF/DAOPHOT software package (Stetson 1987). Final transit light curves were produced by normalizing to a low order polynomial (maximum order 2 in one case, a straight line for all other cases) fitted to the flat part of the light curves that also removes small residual trends if present. The uncertainties in the CAHA and MuSCAT2 light curves are estimated from the point-to-point dispersion of the points out of transit and for all other cases are the combination of the photon noise and the background noise (see the AIJ package; Choi et al. 2016). Nevertheless, as the main source of uncertainties is residual systematics and not photon noise, when fitting the follow-up light curves EXOFASTv2 (see Section 3.2) adds a variance term to each transit to enforce reduced $\chi^2 \sim 1$.

A summary of our follow-up photometric observations is given in Table 1 where we list the date, telescope, filter, and cadence for each transit observation. In the last column we give the mean uncertainty in two-minute bins if the cadence is less

[21] https://www.trappist.uliege.be

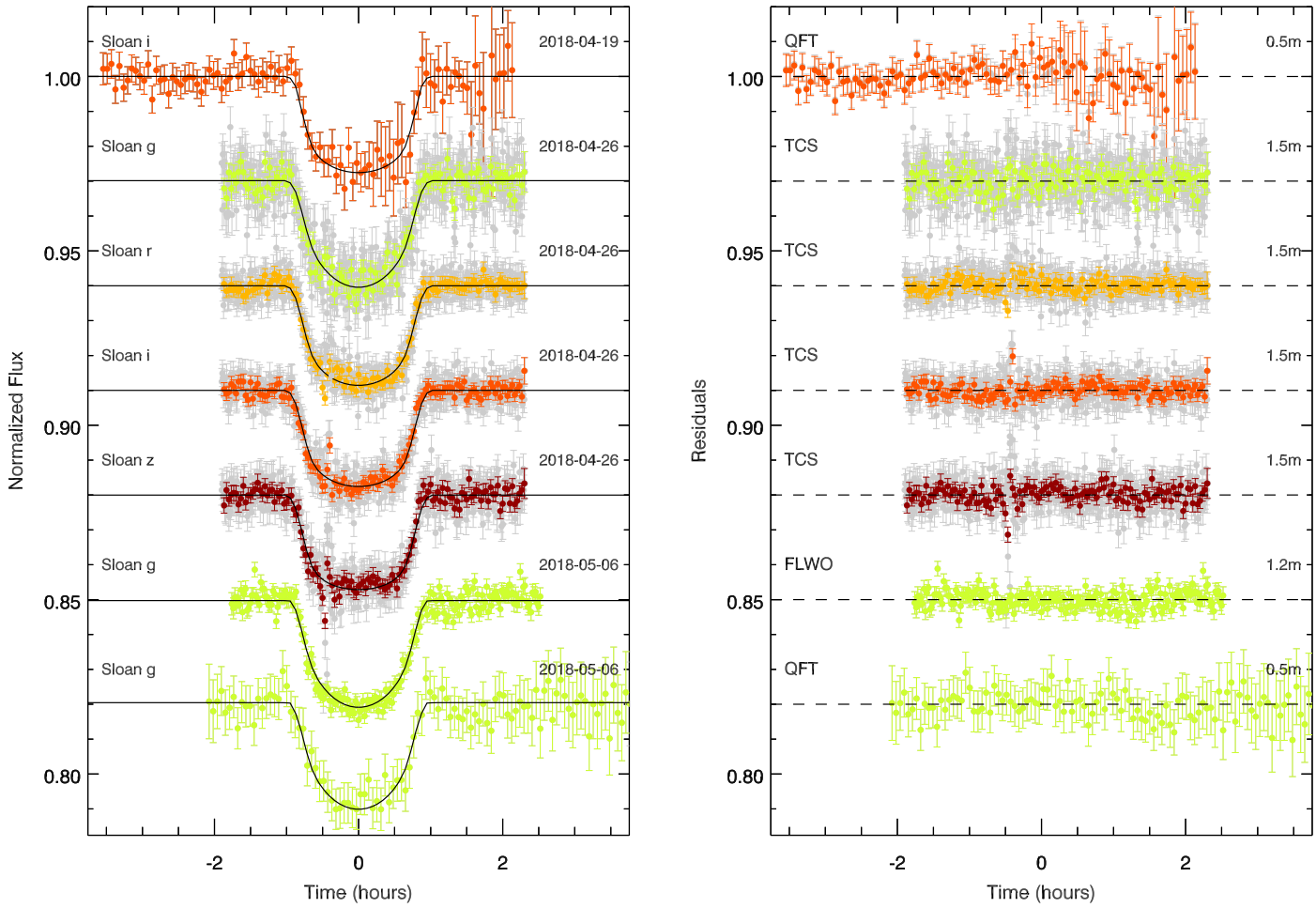

Figure 3. Seven follow-up transit light curves of Qatar-9b. All symbols, labels, and colors follow the same convention as in Figure 2.

Table 2
Relative RVs and BS Variations for Qatar-8

BJD_{TDB}	RV (m s^{-1})	BS (m s^{-1})
TRES		
2458183.747354	22.6 ± 31.4	12.7 ± 14.5
2458207.782751	−113.5 ± 27.0	−28.7 ± 8.8
2458211.702819	−59.5 ± 30.0	3.0 ± 15.5
2458218.684754	−65.5 ± 25.2	6.3 ± 12.3
2458226.645789	−77.7 ± 37.6	35.1 ± 14.8
2458228.646936	20.7 ± 26.3	35.8 ± 14.5
2458241.668589	−80.9 ± 37.2	−12.3 ± 15.8
2458244.754532	−57.5 ± 32.6	−32.1 ± 21.5
2458261.706560	0.0 ± 27.0	12.2 ± 8.0
2458263.738688	−110.5 ± 24.5	−24.9 ± 17.4
2458267.667690	−81.7 ± 20.4	−34.7 ± 15.7
2458274.674490	−64.9 ± 33.0	10.1 ± 17.6
2458276.668550	−7.3 ± 24.1	6.0 ± 11.2
2458278.682960	−44.1 ± 26.3	19.6 ± 17.1
2458280.670353	24.7 ± 20.7	−7.9 ± 12.7
FIES		
2458223.51513	0.0 ± 9.0	14.0 ± 11.0
2458233.50676	−8.1 ± 7.6	38.2 ± 13.6

Table 3
Relative RVs and BS Variations for Qatar-9

BJD_{TDB}	RV (m s^{-1})	BS (m s^{-1})
2458172.753789	−508.1 ± 62.8	−29.4 ± 33.6
2458216.655360	100.7 ± 90.8	55.9 ± 52.8
2458259.747481	−60.5 ± 57.8	−12.5 ± 43.7
2458266.688086	−550.1 ± 37.1	−167.1 ± 29.1
2458273.684727	−43.8 ± 49.5	28.0 ± 34.0
2458276.698788	0.0 ± 57.8	54.4 ± 21.8
2458277.715329	−213.2 ± 74.9	56.3 ± 60.1
2458279.694742	38.7 ± 49.4	−9.1 ± 43.0
2458280.702564	−458.2 ± 40.2	23.6 ± 29.8

than 2 minutes, otherwise for the original observations cadence. The resulting light curves, along with the best model fit and the corresponding residuals, are plotted in Figures 2–4.

2.3. Follow-up Spectroscopy

Follow-up spectroscopic observations to measure precision RVs for all three targets—Qatar-8b, 9b, and 10b—were obtained in the same manner as for all previous QES candidates (for details see Alsubai et al. 2011 and subsequent papers). In brief, we used the Tillinghast Reflector Echelle Spectrograph (TRES) on the 1.5 m Tillinghast Reflector at FLWO. All spectra were obtained using the medium fiber, which results in a resolving power of $R \sim 44{,}000$ and a velocity resolution element of 6.8 km s^{-1} FWHM. The wavelength calibration was established using a Th–Ar hollow-cathode lamp illuminating

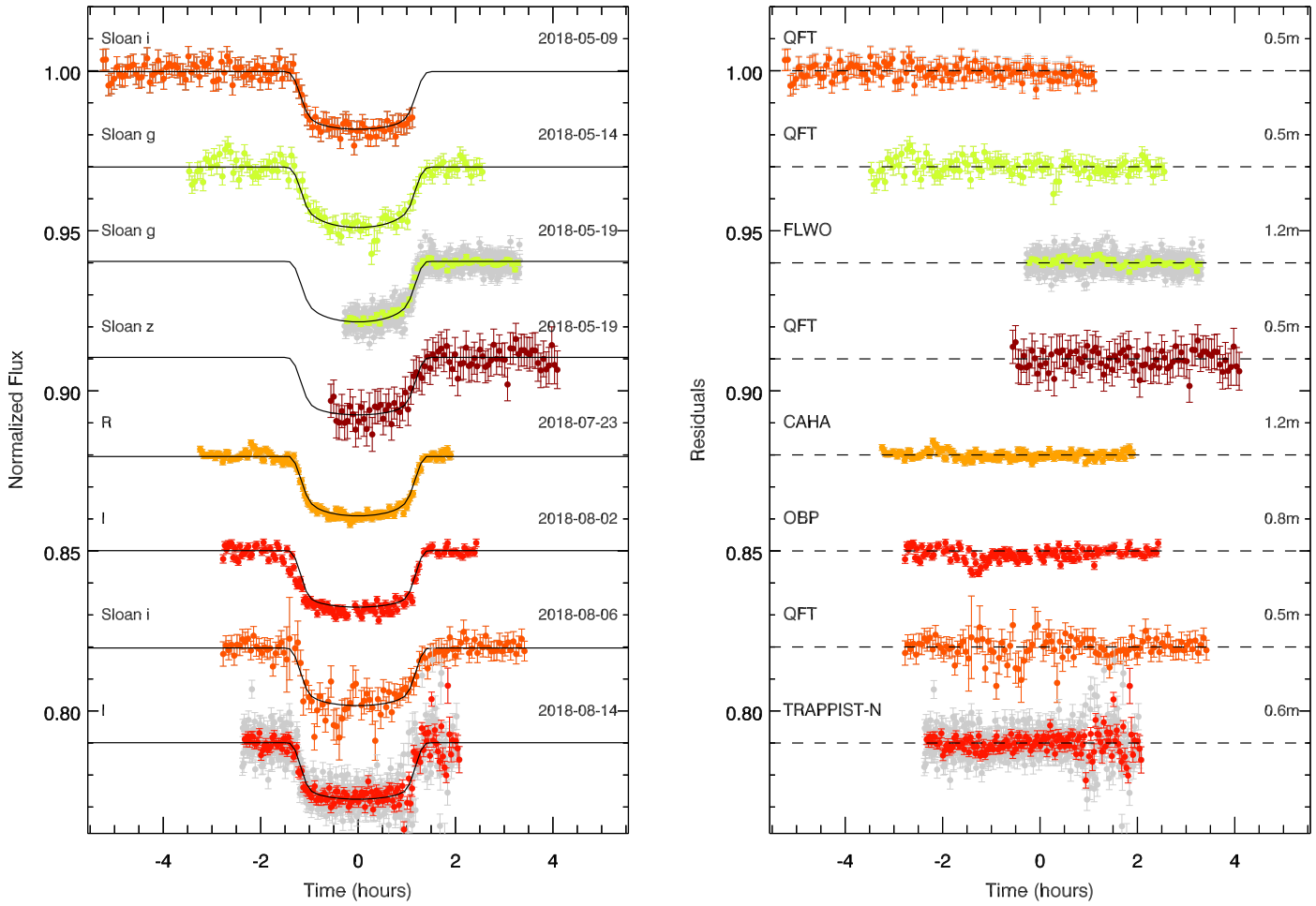

Figure 4. Same as Figures 2 and 3 but for Qatar-10b. All symbols, labels, and colors follow the same convention.

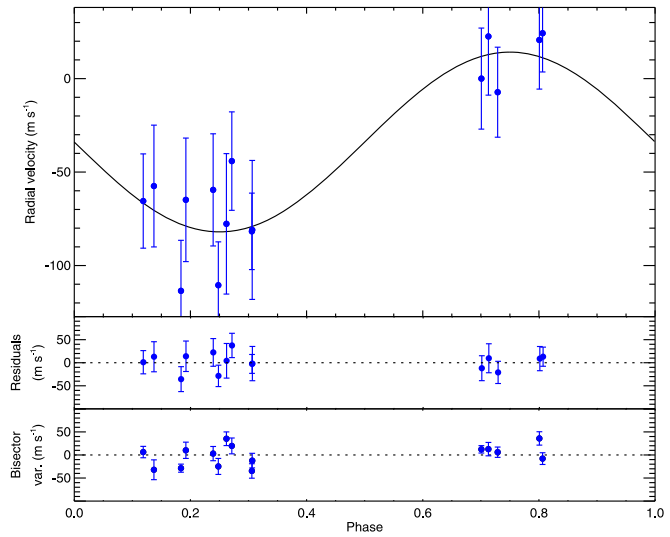

Figure 5. Orbital solution for Qatar-8b, showing the velocity curve and observed velocities and the bisector values.

Table 4
Relative RVs and BS Variations for Qatar-10

BJD_{TDB}	RV (m s^{-1})	BS (m s^{-1})
2458258.976713	10.2 ± 36.9	18.3 ± 15.2
2458259.824390	−179.3 ± 42.7	−19.8 ± 19.1
2458263.950937	−37.0 ± 28.7	−31.0 ± 19.0
2458273.912527	0.0 ± 34.9	−29.1 ± 9.0
2458274.928598	−175.8 ± 34.9	−28.0 ± 15.8
2458277.931350	−216.8 ± 39.2	−20.9 ± 19.8
2458278.755400	57.9 ± 39.3	38.5 ± 30.2
2458280.931487	−170.8 ± 30.0	−24.8 ± 15.4
2458281.917044	55.7 ± 23.3	6.6 ± 15.9
2458292.804140	−204.4 ± 34.8	−3.7 ± 11.9
2458296.861241	152.0 ± 38.2	64.4 ± 31.0
2458300.930706	−232.4 ± 33.5	15.3 ± 16.6
2458301.790512	39.0 ± 33.1	14.8 ± 16.6
2458386.632867	−174.7 ± 30.1	40.9 ± 21.0
2458387.655367	−13.7 ± 32.6	−10.0 ± 18.6
2458389.611784	−130.1 ± 37.6	−49.1 ± 20.5

the science fiber with two exposures obtained immediately before and after each target spectrum.

For each one of the three target stars we obtained the following TRES spectra: (a) Qatar-8–15 spectra between 2017 March 6 and 2018 June 11 with exposure times in the range of 10–30 minutes and an average signal-to-noise ratio per resolution element (SNRe) ∼34 at the peak of the continuum in the echelle order centered on the Mg b triplet near 519 nm; (b) Qatar-9–9 spectra between 2018 February 23 and June 11 all with individual exposure times of 60 minutes and an average

Table 5
Basic Observational and Spectroscopic Parameters of Qatar-8b, 9b, 10b Host Stars and Photometry Used for the Spectral Energy Distribution Fit

Parameter	Description	Value			References
Names		Qatar-8b	Qatar-9b	Qatar-10b	
	3UC	322-045544	302-100935	320-060170	
	2MASS	J23540364+3701185	J23540364+3701185	J23540364+3701185	
Astrometry					
α_{2000}	R.A. (J2000)	$10^h29^m38^s.962$	$10^h42^m59^s.543$	$18^h57^m46^s.537$	(1)
δ_{2000}	decl. (J2000)	$+70°31'37''.50$	$+60°57'50''.83$	$+69°34'15''.01$	(1)
Photometry					
B	Johnson B, mag	12.132 ± 0.084	15.515 ± 0.088	13.437 ± 0.080	(2)
V	Johnson V, mag	11.526 ± 0.046	14.133 ± 0.048	12.879 ± 0.079	(2)
g	Sloan g, mag	11.806 ± 0.018	14.894 ± 0.065	13.147 ± 0.124	(2)
r	Sloan r, mag	11.355 ± 0.028	13.569 ± 0.061	12.712 ± 0.079	(2)
i	Sloan i, mag	11.174 ± 0.015	13.074 ± 0.078	12.569 ± 0.109	(2)
J	2MASS J, mag	10.299 ± 0.023	11.835 ± 0.019	11.754 ± 0.022	(3)
H	2MASS H, mag	10.005 ± 0.024	11.235 ± 0.017	11.474 ± 0.023	(3)
K	2MASS K, mag	9.937 ± 0.015	11.104 ± 0.023	11.382 ± 0.017	(3)
$W1$	*WISE*1, mag	9.890 ± 0.023	11.021 ± 0.024	11.375 ± 0.023	(4)
$W2$	*WISE*2, mag	9.932 ± 0.021	11.120 ± 0.021	11.413 ± 0.020	(4)
$W3$	*WISE*3, mag	9.902 ± 0.033	10.986 ± 0.090	11.348 ± 0.067	(4)
Spectroscopic Parameters					
	Spectral type	G0V	K5V	F7V	this work
$T_{\rm eff}$	Effective temperature, K	5687 ± 50	4363 ± 51	6123 ± 50	this work
log g	Gravity, cgs	4.22 ± 0.10	4.65 ± 0.10	4.36 ± 0.10	this work
[m/H]	Metallicity	0.0 ± 0.08	0.25 ± 0.08	0.40 ± 0.08	this work
$\gamma_{\rm abs}$	Systemic velocity, km s^{-1}	5.57 ± 0.10	2.92 ± 0.10	−25.49 ± 0.10	this work
$v_{\rm rot}$	Rotational velocity, km s^{-1}	2.7 ± 0.5	4.3 ± 0.5	5.9 ± 0.5	this work

References. (1) *GAIA* DR2 http://gea.esac.esa.int/archive/; (2) APASS9 http://www.aavso.org/apass; (3) 2MASS http://irsa.ipac.caltech.edu/Missions/2mass.html; (4) *WISE* http://irsa.ipac.caltech.edu/Missions/wise.html.

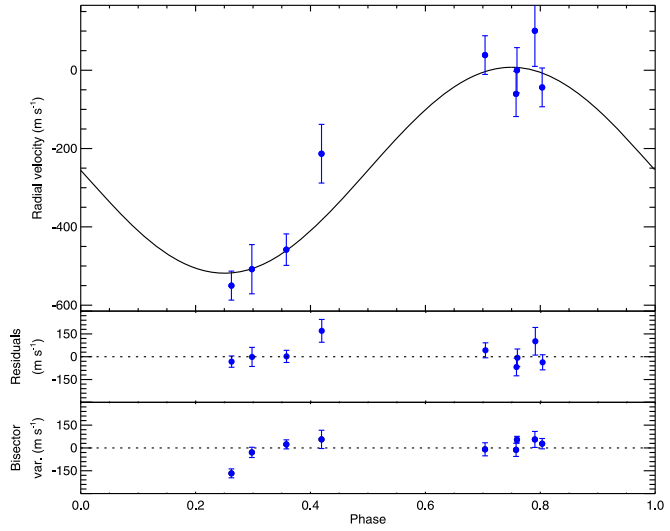

Figure 6. Orbital solution for Qatar-9b, showing the velocity curve and observed velocities and the bisector values.

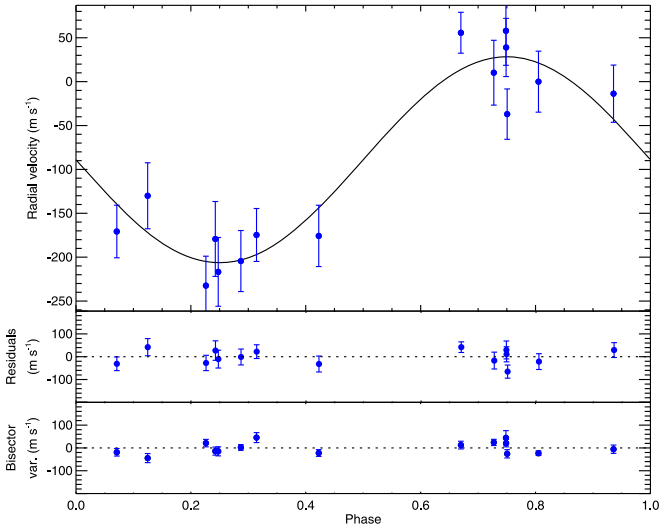

Figure 7. Orbital solution for Qatar-10b, showing the velocity curve and observed velocities and the bisector values.

SNRe ∼14.9; (c) Qatar-10–16 spectra between 2018 May 20 and September 28, with exposure times in the range of 20–40 minutes and an average SNRe ∼30. For each of our target stars, we cross-correlated each observed spectrum against the reference spectrum (taken to be the strongest among the spectra of the given star) to obtain relative RVs. This was done for a set of echelle orders (in an order-by-order fashion) chosen so as to have both good SNRe and minimal telluric line contamination. These RVs are reported in Tables 2–4 (with the time stamps in Barycentric Julian Date in Barycentric Dynamical time, BJD_{TDB}) and plotted in Figures 5–7. The observation that was used for the template spectrum has, by definition, an RV of 0.0 km s^{-1}, and the error on the template RV is the median of the uncertainties of all the orders. In order to be sure that the periodic RV signal detected in all three cases is due to orbital motion and excludes other astrophysical phenomena that could potentially produce a similar periodic signal, we also derived the line profile bisector span values (BS;

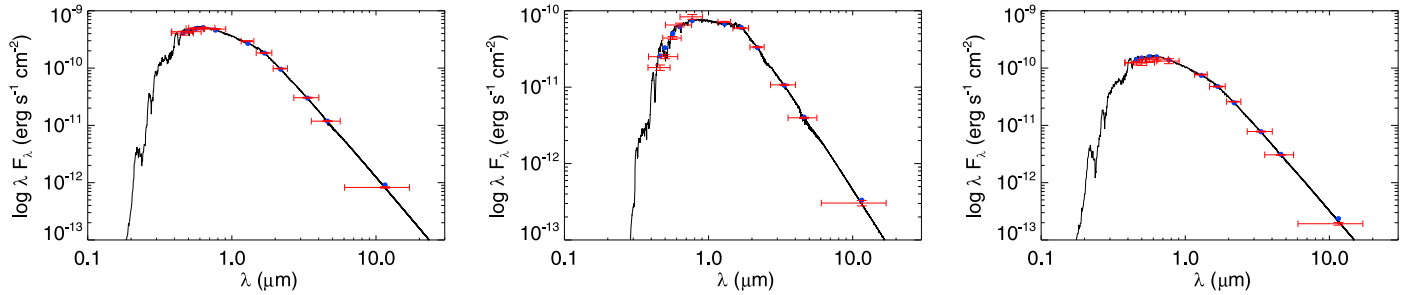

Figure 8. Spectral energy distribution fit for the hosts stars of Qatar-8b (left panel), Qatar-9b (middle panel), and Qatar-10b (right panel). Photometric measurements used in each fit (Table 5) are plotted here as error bars, where the vertical bars represent the quoted 1σ measurement uncertainties, and the horizontal bars mark the effective width of the passbands. The solid curve is the best-fit SED from the NextGen library of models from the global EXOFASTv2 fit.

Table 6
Median Values and 68% Confidence Intervals

Parameter	Units	Qatar-8b	Qatar-9b	Qatar-10b
Stellar Parameters:				
M_*	Mass ($M_\odot$)	1.029 ± 0.051	0.719 ± 0.024	1.156 ± 0.068
R_*	Radius ($R_\odot$)	1.315 ± 0.020	0.696 ± 0.008	1.254 ± 0.026
L_*	Luminosity ($L_\odot$)	1.690 ± 0.068	0.151 ± 0.004	1.993 ± 0.094
ρ_*	Density (g cm^{-3})	0.641 ± 0.024	3.015 ± 0.086	0.823 ± 0.062
$\log(g_*)$	Surface gravity (cgs)	4.214 ± 0.016	4.610 ± 0.010	4.303 ± 0.027
$T_{\rm eff}$	Effective temperature (K)	5738 ± 51	4309 ± 31	6124 ± 46
[Fe/H]	Metallicity	0.025 ± 0.071	0.252 ± 0.076	0.016 ± 0.089
$\tau_{\rm MIST}$	Age (Gyr)	8.3 ± 2.1	7.5 ± 4.5	3.2 ± 1.9
A_V	Extinction (mag)	0.063 ± 0.042	0.016 ± 0.010	0.119 ± 0.062
π	Parallax (mas)	3.614 ± 0.043	4.730 ± 0.036	1.855 ± 0.035
d	Distance (pc)	276.7 ± 3.4	211.4 ± 1.6	539 ± 10
Planetary Parameters:				
P	Period (days)	3.71495 ± 0.00100	1.540731 ± 0.000038	1.645321 ± 0.000010
a	Semimajor axis (au)	0.0474 ± 0.0008	0.0234 ± 0.0003	0.0286 ± 0.0006
$M_{\rm P}$	Mass ($M_{\rm J}$)	0.371 ± 0.062	1.19 ± 0.16	0.736 ± 0.090
$R_{\rm P}$	Radius ($R_{\rm J}$)	1.285 ± 0.022	1.009 ± 0.014	1.543 ± 0.040
$\rho_{\rm P}$	Density (g cm^{-3})	0.216 ± 0.037	1.43 ± 0.20	0.248 ± 0.036
$\log(g_{\rm P})$	Surface gravity	2.745 ± 0.080	3.460 ± 0.063	2.884 ± 0.059
$T_{\rm eq}$	Equilibrium Temperature (K)	1457 ± 14	1134 ± 9	1955 ± 25
Θ	Safronov Number	0.0265 ± 0.0044	0.0764 ± 0.0100	0.0236 ± 0.0028
RV Parameters:				
K	RV semi-amplitude (m s^{-1})	47.7 ± 8.0	259 ± 35	114 ± 13
$\gamma_{\rm rel}$	Relative RV offset, TRES (m s^{-1})	−34.2 ± 6.8	−252 ± 32	−89 ± 11
$\gamma_{\rm rel}$	Relative RV offset, FIES (m s^{-1})	25 ± 13		
e	Eccentricity (fixed)	0	0	0
Primary Transit Parameters:				
$T_{\rm C}$	Time of transit ($\rm BJD_{TDB}$)	2458210.83980 ± 0.00085	2458227.75643 ± 0.00027	2458247.90746 ± 0.00036
$R_{\rm P}/R_\star$	Radius of planet in stellar radii	0.1005 ± 0.0008	0.1489 ± 0.0009	0.1265 ± 0.0010
$a/R_\star$	Semimajor axis in stellar radii	7.761 ± 0.100	7.236 ± 0.069	4.90 ± 0.12
i	Inclination (°)	89.29 ± 0.70	89.23 ± 0.64	85.87 ± 0.96
b	Impact Parameter	0.096 ± 0.093	0.097 ± 0.079	0.379 ± 0.055
T_{14}	Total duration (days)	0.1678 ± 0.0017	0.0778 ± 0.0004	0.1155 ± 0.0009

lower panels in Figures 5–7). Buchhave et al. (2010) describe the procedures used above for both the RV and the BS measurements in more detail. The absolute center-of-mass velocity of each system is determined in two steps as the precise RV of each spectrum is measured against the strongest observed spectrum of the same star. That reference spectrum could be anywhere on the RV curve, and so a relative systemic velocity ($\gamma_{\rm rel}$) is determined when fitting the Keplerian model. The absolute systemic velocity is then the sum of $\gamma_{\rm rel}$ and the absolute RV offset of the reference spectrum which is determined by cross-correlating the Mg b order of the respective reference spectrum against the CfA library of synthetic templates. We also correct by $-0.61\,{\rm km\,s^{-1}}$, because the CfA library does not include the gravitational redshift. This offset has been determined empirically by many observations of IAU Radial Velocity Standard Stars system. We quote an uncertainty of $\pm 0.1\,{\rm km\,s^{-1}}$ in the resulting absolute velocity, which is an estimate of the residual systematic errors in the IAU Radial Velocity Standard Star system. Note that the error in determining the absolute center-of-mass RV of each system does not affect the determination of the planetary parameters. Although a dedicated paper on the assessment of the TRES absolute zero-point has not been published, we refer the interested reader to

Quinn et al. (2014, 2015), which gives a detailed account of the instrument RV precision, stability, sources of error, and steps used to bring observed stellar velocities to the absolute scale of the IAU Radial Velocity Standard Star system.

For Qatar-8 we also obtained two RV measurements, on 2018 April 15 and 25, with the high-resolution Fiber-fed Echelle Spectrograph (FIES; Telting et al. 2014) on the 2.5 m Nordic Optical Telescope (NOT) at the Observatorio del Roque de los Muchachos (ORM) on the island of La Palma, Canary Islands, Spain. We used FIES in its high-resolution mode $R \sim 67{,}000$ and a velocity resolution element of 4.8 km s^{-1} FWHM. For the first observation we obtained a single 30-minute exposure spectrum, while for the second observation we obtained three consecutive 15-minute exposure spectra. Similar to the TRES observations, the wavelength calibration was established using exposures of a Th–Ar lamp illuminating the science fiber bracketing the target exposure spectra. Relative RV measurements were obtained through the cross-correlation technique described above and using the spectrum obtained on 2018 April 15 ($T_{\rm exp} = 30$ minutes) as a template. Each one of the three spectra obtained on 2018 April 25 was measured separately against the template and the three measurements were averaged.

3. Analysis and Results

3.1. Rejecting False Positives

For all three targets, the observed transit light curves combined with the shape and amplitude of the RV variations, are well described by a planet orbiting a single star. Nevertheless, there are astrophysical scenarios not involving a planet that could mimic such a behavior. These include an eclipsing binary—either a background or in a hierarchical triple system—blended with the primary, much brighter star. Next we put forward arguments that allow us to exclude such scenarios.

It has been well established (e.g., Queloz et al. 2001; Torres et al. 2005) that if the observed RV pattern were a result of a blend with an eclipsing binary, the spectral line bisectors (see Tables 2–4) would follow a similar pattern, that is, they would vary in phase with the photometric period and with a similar amplitude. The measured line bisectors are shown in the bottom panels in Figures 5–7 on the same scale as the RV residuals from the Keplerian orbit fit. No obvious pattern is seen in all three cases. To quantify that we performed a significance test on the Pearson's correlation between the BS and RV for each star, and also the BS and the Keplerian fit model. In each of the three cases, the correlation between the BS and the RV (or between the BS and the Keplerian model) is insignificant, while the correlation between the RV and the Keplerian model is highly significant. Numerically, the probability of chance RS/RV correlation is higher than the typical significance level (5%): Qatar-8b—p-values, $p = 0.061$; Qatar-9b—$p = 0.073$; Qatar-10b—$p = 0.067$. This supports our argument that the observed RV pattern is a result of a gravitationally induced motion from a planet orbiting a single star.

A further argument in favor of the planet scenario can be drawn from the equal transit depths across all filters (accounting for limb-darkening effects). We do, however, note that an eclipse of a stellar companion with very similar colors would also lead to equal depths at different wavelengths. As such, we consider the equal depths as a supportive argument only, albeit in full agreement with our conclusion regarding the planetary nature of the transits.

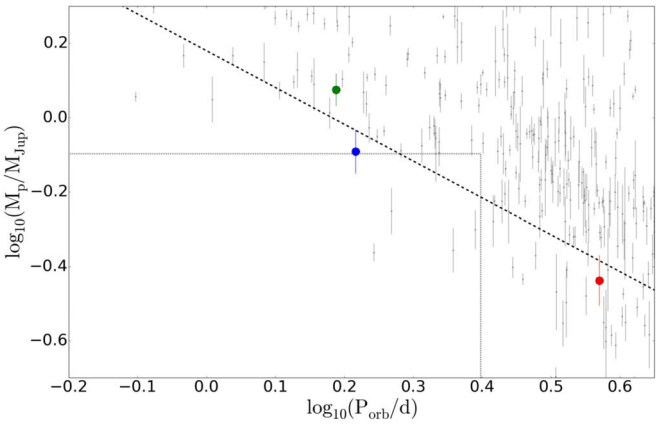

Figure 9. Orbital period vs. planet mass. The planets data (gray points) are from TEPCat, while Qatar-8b, 9b, and 10b are plotted as the red, green, and blue points, respectively. The dotted box is the sub-Jupiter desert as defined by Szabó & Kiss (2011), while the dashed line is the upper limit of the same, as defined by Mazeh et al. (2016).

3.2. Planetary System Parameters

Physical properties of each system were determined through a global model fit using the EXOFASTV2 package. A detailed description of EXOFASTV2 can be found in Eastman (2017) and Rodriguez et al. (2017). For each of the three exoplanetary systems the global fit includes the RV measurements listed in Tables 2–4, the follow-up transit light curves shown in Figures 2–4, respectively, the distance and broadband photometry for each star, and the priors on the stellar atmospheric parameters ($T_{\rm eff}$ and [Fe/H]) determined from the available spectra.

The effective temperature ($T_{\rm eff}$), surface gravity ($\log g$), metallicity ([m/H]), and projected rotational velocity ($v_{\rm rot}$) for the host stars were determined using the stellar parameter classification tool (SPC; Buchhave et al. 2012). SPC works by cross-correlating an observed spectram against a grid of synthetic spectra based on the Kurucz atmospheric models. We used the ATLAS9 grid of models with the opacity distribution functions from Castelli & Kurucz (2004). In Table 5 we list the weighted mean values and the associated uncertainties of the stellar atmospheric parameters determined from the SPC analysis of each individual spectrum.

Broadband photometric surveys provide measurements across the electromagnetic spectrum for all three host stars, from the optical (APASS) to the mid-IR (*WISE*). These measurements are gathered in Table 5 and used to fit a model spectral energy distribution (SED) for each one of the stars as described below. The resulting SED fits are shown in Figure 8.

In the global fit we apply Gaussian priors on the parallax from *Gaia* DR2, including the offset determined by Stassun & Torres (2016) and impose an upper limit on the V-band extinction from the Galactic dust reddening maps (Schlafly & Finkbeiner 2011). The limb-darkening coefficients were fit with a prior derived from an interpolation from the Claret & Bloemen (2011) tables for each band. We note that while all transit light curves were normalized as described in Section 2.2, in the global fit EXOFASTV2 treats the baseline flux (the flux outside the transit) as a free constant and adjusts its value to unity. Because all transit light curves were normalized in advance this adjustment is naturally very small.

All of the host stars properties were determined during the global fit. EXOFASTV2 simultaneously uses the SED, the stellar

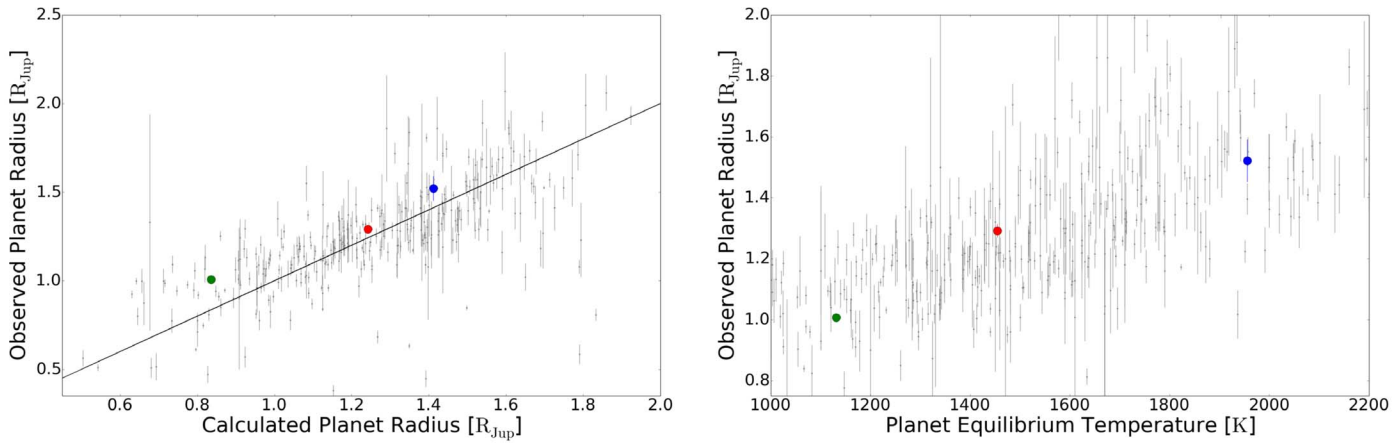

Figure 10. Left panel: theoretical planetary radii, calculated from Enoch et al. (2012), vs. observed planetary radii. Right panel: planetary equilibrium temperatures vs. observed planetary radii. As in Figure 9, in both panels, gray points are data from TEPCat, while the red, green, and blue points represent Qatar-8b, 9b, and 10b, respectively.

density and limb-darkening constraint from the transit, the MIST isochrones (Collier Cameron et al. 2006; Dotter 2016), priors from SPC ($T_{\rm eff}$, [Fe/H]) and *Gaia* (parallax), and an upper limit on the reddening to simultaneously determine all the stellar properties. The stellar radius is predominantly constrained by the SED and *Gaia* parallax, while the stellar age and mass are predominantly constrained by the MIST isochrones and spectroscopic priors. In addition, consistency between the stellar mass and radius derived from these methods and the stellar density from the transit is strictly required.

In fitting Qatar-8b, 9b, and 10b we only considered circular orbits and kept the eccentricity fixed to zero. On the one hand, our RV data is not of high enough quality to allow investigation of potential small departures from circularity, and on the other hand we expect the planets orbits to have circularized. Following the equations from Jackson et al. (2008), and using the values from Table 6 of $M_\star$, $R_\star$, $M_{\rm P}$, $R_{\rm P}$, and $a/R_\star$, we estimate orbit circularization timescales of $\tau_{\rm circ} \sim 0.04$, 0.01, 0.01 Gyr, respectively, for the entire range of tidal quality factors $Q_\star$ and $Q_{\rm P}$ considered by the authors (10^4–10^8 for each Q). This is much lower than the estimated age of the host stars and, thus, we expect the planet orbit to have circularized.

A precise orbital period for each system is also obtained during the global fit. The best ephemeris for each star is calculated by fitting all transits simultaneously to a linear ephemeris within EXOFASTV2:

$$T_{\rm C} = 2458210.83980(85) + 3.71495(100)E, \quad (1)$$

$$T_{\rm C} = 2458227.75643(27) + 1.540731(38)E, \quad (2)$$

$$T_{\rm C} = 2458247.90746(36) + 1.645321(10)E, \quad (3)$$

where E is the number of cycles after the reference epoch, which we take to be the transit time that minimizes the covariance between $T_{\rm C}$ and the period, and the numbers in parenthesis denote the uncertainty in the last two digits. Equations (1)–(3) correspond to Qatar-8b, 9b, and 10b, respectively.

Table 6 summarizes the physical parameters of each planetary system. We note that for Qatar-8b, for which we have RV measurements from two different telescopes and instruments, EXOFASTV2 fits the relative offset for each RV data set separately. These are the reported $\gamma_{\rm rel}$ values in the table. The Safronov number is not used in the current paper and is provided in Table 6 for completeness, as it may be useful for other studies.

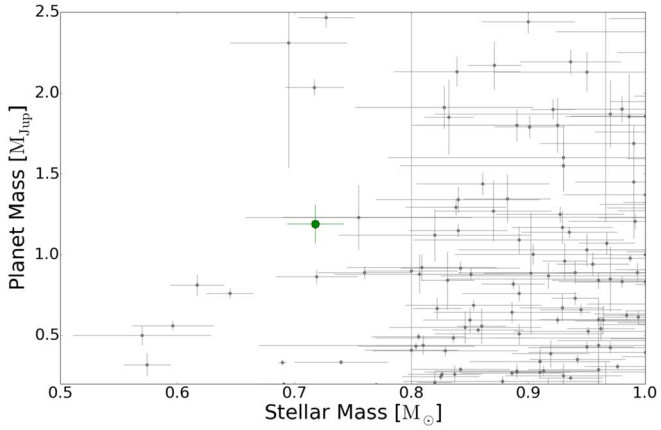

Figure 11. Stellar mass vs. planet mass, illustrating the scarcity of Jupiter and super-Jupiter mass planets around low mass hosts $M_* < 0.8\,M_\odot$. Gray points are data from TEPCat, while the larger green point indicates Qatar-9b.

4. Discussion and Conclusions

In this paper we present Qatar-8b, 9b, and 10b, a transiting hot Saturn and two transiting hot Jupiters identified by QES. We combine follow-up photometric and spectroscopic observations, together with available broadband photometry and *GAIA* measurements, to calculate a full set of physical parameters for the planets and their host stars. In Figures 9 and 10 we present the new discoveries in the context of the current state of the field. To produce these figures, we made use of the well-studied sample of planets from the Transiting Extrasolar Planets Catalogue (TEPCat; Southworth 2011, online version[22] as of 2018 October 10).

Qatar-8b is a typical example of a hot Saturn, Qatar-9b is slightly more massive than Jupiter itself, but with a similar radius, and Qatar-10b is a sub-Jupiter mass planet, very similar to HATS-9b (Brahm et al. 2015) and WASP-142b (Hellier et al. 2017). In the left panel of Figure 10 we present a predicted versus observed planetary radii plot based on the

[22] http://www.astro.keele.ac.uk/jkt/tepcat/

widely used relations of Enoch et al. (2012). At face value, the relations of Enoch et al. (2012) underpredict the observed radius of Qatar-9b, while the observed radii of Qatar-8b and Qatar-10b are close to the theoretical predictions. We note however, that none of the three new exoplanets stand out from the rest and follow the general trend well.

An interesting aspect of Qatar-9b is the moderately large planet mass, $M_P = 1.19\ M_J$, in relation to the relatively low host star mass, $M_\star = 0.72\ M_\odot$. Using data from TEPCat, we find 59 planets with a host mass of $M_\star < 0.8\ M_\odot$ and only 8 of these have masses in the range of $0.7 \leqslant M_P\,[M_J] \leqslant 2.5$. The position of Qatar-9b in this scarcely populated region of the parameter space is shown in Figure 11. We also note that Qatar-10b, at an orbital period of 1.65 days, is situated on the upper edge of the sub-Jupiter desert (e.g., Szabó & Kiss 2011; Mazeh et al. 2016; and see again Figure 9).

The combination of relatively low surface gravity and relatively high equilibrium temperature for both Qatar-8b and Qatar-10b imply considerable-sized atmospheres. The atmospheric scale height, given by $H = kT/g\mu$ and assuming a Jupiter mean molecular mass of 2.3 times the mass of a proton, is calculated to be ∼930 km for Qatar-8b and ∼850 km for Qatar-10b. Taking into account the somewhat large host radii, the absorption signal, A, of an annular area of one atmospheric scale height during transit (Brown 2001) is calculated to be ∼200 ppm and ∼250 ppm for Qatar-8b and 10b, respectively.

This publication is supported by NPRP grant No. X-019-1-006 from the Qatar National Research Fund (a member of Qatar Foundation). The statements made herein are solely the responsibility of the authors. The Nanshan 1 m telescope of XAO is supported by the CAS "Light of West China" program (XBBS-2014-25, 2015-XBQN-A-02), and the Youth Innovation Promotion Association CAS (2014050). This article is partly based on observations made with the MuSCAT2 instrument, developed by ABC, at Telescopio Carlos Sánchez operated on the island of Tenerife by the IAC in the the Spanish Observatorio del Teide. This work is partly financed by the Spanish Ministry of Economics and Competitiveness through grants ESP2013-48391-C4-2-R. TRAPPIST-North is a project funded by the University of Liège, and performed in collaboration with Cadi Ayyad University of Marrakesh. The research leading to these results has received funding from an ARC grant for Concerted Research Actions financed by the Wallonia-Brussels Federation. M.G. and E.J. are F.R.S.-FNRS Senior Research Associates. L.M. acknowledges support from the Italian Minister of Instruction, University and Research (MIUR) through FFABR 2017 fund and from the University of Rome Tor Vergata through "Mission: Sustainability 2016" fund. This work has made use of data from the European Space Agency (ESA) mission *Gaia* (https://www.cosmos.esa.int/gaia), processed by the *Gaia* Data Processing and Analysis Consortium (DPAC; https://www.cosmos.esa.int/web/gaia/dpac/consortium). Funding for the DPAC has been provided by national institutions, in particular the institutions participating in the *Gaia* Multilateral Agreement. We also acknowledge support from JSPS KAKENHI grant No. JP16K13791, 17H04574, 18H01265, and 18H05439, and JST PRESTO grant No. JPMJPR1775.

ORCID iDs

Khalid Alsubai https://orcid.org/0000-0001-6253-0179
Zlatan I. Tsvetanov https://orcid.org/0000-0001-6177-6767
David W. Latham https://orcid.org/0000-0001-9911-7388
Allyson Bieryla https://orcid.org/0000-0001-6637-5401
Jason Eastman https://orcid.org/0000-0003-3773-5142
Dimitris Mislis https://orcid.org/0000-0003-4819-1435
Luigi Mancini https://orcid.org/0000-0002-9428-8732
Pilar Montañes-Rodriguez https://orcid.org/0000-0002-6855-9682
Norio Narita https://orcid.org/0000-0001-8511-2981
Akihiko Fukui https://orcid.org/0000-0002-4909-5763
Motohide Tamura https://orcid.org/0000-0002-6510-0681
Francisco Pozuelos https://orcid.org/0000-0003-1572-7707
Michael Gillon https://orcid.org/0000-0003-1462-7739

References

Alonso, R., Brown, T. M., Torres, G., et al. 2004, ApJL, 613, L153
Alsubai, K., Mislis, D., Tsvetanov, Z. I., et al. 2017, AJ, 153, 200
Alsubai, K., Parley, N. R., Bramich, D. M., et al. 2011, MNRAS, 417, 709
Alsubai, K., Parley, N. R., Bramich, D. M., et al. 2013, AcA, 63, 465
Alsubai, K., Tsvetanov, Z. I., Latham, D. W., et al. 2018, AJ, 155, 52
Bakos, G., Noyes, R. W., Kovács, G., et al. 2004, PASP, 116, 266
Barklem, P. S., Stempels, H. C., Allende Prieto, C., et al. 2002, A&A, 385, 951
Brahm, R., Jordán, A., Hartman, J. D., et al. 2015, AJ, 150, 33B
Bramich, D. M. 2008, MNRAS, 386, L77
Brown, D. J. A. 2014, MNRAS, 442, 1844
Brown, T. M. 2001, ApJ, 553, 1006B
Buchhave, L. A., Bakos, G. Á., Hartman, J. D., et al. 2010, ApJ, 720, 1118
Buchhave, L. A., Latham, D. W., Johansen, A., et al. 2012, Natur, 486, 375
Castelli, F., & Kurucz, R. L. 2004, in IAU Symp. 210, Modelling of Stellar Atmospheres, Poster Contributions, ed. N. Piskunov, W. W. Weiss, & D. F. Gray (Cambridge: Cambridge Univ. Press), A20
Choi, J., Dotter, A., Conroy, C., et al. 2016, ApJ, 823, 102
Claret, A., & Bloemen, S. 2011, A&A, 529, 75
Collier Cameron, A., Pollacco, D., Street, R. A., et al. 2006, MNRAS, 373, 799
Dotter, A. 2016, ApJS, 222, 8
Eastman, J. 2017, EXOFASTv2, Generalized publication-quality exoplanet modeling code, Astrophysics Source Code Library, ascl:1710.003
Enoch, B., Collier Cameron, A., & Horne, K. 2012, A&A, 540A, 99E
Hellier, C., Anderson, D. R., Collier Cameron, A., et al. 2017, MNRAS, 465, 3693H
Henden, A. A., Levine, S., Terrell, D., & Welch, D. L. 2015, AAS Meeting, 225, 336.16
Jackson, B., Greenberg, R., & Barnes, R. 2008, ApJ, 678, 1396
Kovács, G., Bakos, G., & Noyes, R. 2005, MNRAS, 356, 557
Kovács, G., Zucker, S., & Mazeh, T. 2002, A&A, 391, 369
Mayor, M., & Queloz, D. 1995, Natur, 378, 355
Mazeh, T., Holczer, T., & Faigler, S. 2016, A&A, 589, A75
McCullough, P. R., Stys, J. E., Valenti, J. A., et al. 2005, PASP, 117, 783
Meléndez, J., Bergemann, M., Cohen, J. G., et al. 2012, A&A, 543, A29
Meléndez, J., Bergemann, M., Cohen, J. G., et al. 2014, A&A, 567, L3
Mislis, D., Pyrzas, S., Alsubai, K. A., et al. 2017, MNRAS, 465, 3759M
Mislis, D., Pyrzas, S., Alsubai, K. A., et al. 2018, MNRAS, 481, 1624M
Narita, N., Fukui, A., Kusakabe, N., et al. 2019, JATIS, 5, 015001
Pepper, J., Pogge, R. W., DePoy, D. L., et al. 2007, PASP, 119, 923
Pollacco, D. L., Skillen, I., Collier Cameron, A., et al. 2006, PASP, 118, 1407
Queloz, D., Henry, G. W., Sivan, J. P., et al. 2001, A&A, 379, 279
Quinn, S. N., White, R. J., Latham, D. W., et al. 2014, ApJ, 787, 27
Quinn, S. N., White, T. R., Latham, D. W., et al. 2015, ApJ, 803, 49
Rodriguez, J. E., Zhou, G., Vanderburg, A., et al. 2017, AJ, 153, 256
Schlafly, E. F., & Finkbeiner, D. P. 2011, ApJ, 737, 103
Southworth, J. 2011, MNRAS, 417, 2166
Southworth, J., Hinse, T. C., Burgdorf, M., et al. 2014, MNRAS, 444, 776
Southworth, J., Hinse, T. C., Jørgensen, U. G., et al. 2009, MNRAS, 396, 1023
Stassun, K. G., & Torres, G. 2016, ApJ, 831, 6
Stetson, P. B. 1987, PASP, 99, 191
Szabó, G. M., & Kiss, L. L. 2011, ApJ, 727L, 44S
Telting, J. H., Avila, G., Buchhave, L., et al. 2014, AN, 335, 41
Torres, G., Andersen, J., & Giménez, A. 2010, A&ARv, 18, 67
Torres, G., Konacki, M., Sasselov, D., & Jha, S. 2005, ApJ, 619, 558
Tucci Maia, M., Meléndez, J., Castro, M., et al. 2015, A&A, 576, L10
Udalski, A., Paczynski, B., Zebrun, K., et al. 2002, AcA, 52, 1